Flow Induced Birefringence Study of Secondary Flow in Entrance Region of Rectangular Slit Channel for Long-chain-branched Polyethylene Melt

Jan Musil and Martin Zatloukal*

Polymer Centre, Faculty of Technology, Tomas Bata University in Zlín, Vavrečkova 275, 760 01 Zlín, Czech Republic

*corresponding author: mzatloukal@utb.cz

Abstract

This work presents an analysis of the inner boundary of the secondary flow (i.e. corner vortex flow) in entrance region of rectangular slit channel for long-chain-branched polyethylene melt evaluated using particle tracking and stress-induced birefringence measurements. Further, the flow-induced birefringence technique was used to investigate the effects of temperature and shear rate on the size of the secondary entry flow. Obtained results and trends were compared with the laser-Doppler velocimetry data taken from the open literature for the same polymer melt and comparable flow conditions. Interestingly, the results of both methods were very similar. This suggests that the stress-induced birefringence measurements may be a useful tool for investigating secondary entry flows of polymer melts.

Keywords: Flow instabilities, Secondary flows, Vortex formation, Flow visualization, Flow induced birefringence, Planar extensional viscosity, Polymer extrusion.

INTRODUCTION

Understanding the flow behaviour of viscoelastic fluids in confined geometries is essential for applications in polymer melt/solution processing [1-4], processing of biological/medical systems [5-7], enhanced oil recovery [8-10], dampers [11-13] and many others. Historically, Tordella [14] in 1957 was the first to attempt to visualize the die entry flow region during his original work on melt fracture research. He extruded low-density polyethylene (LDPE) filled with a small amount of hard carbon black particles as flow tracers through a circular glass capillary and first observed that "Several black particles occurred in the volume of polymer near the glass inlet…circulated but did not flow out…Near the capillary the trapped polymer flowed away from the capillary, up the cylinder, and then down again near the interface." This new unstable rheological phenomenon is today known as "*secondary flow(s)*", "*stagnation flow(s)*", "*dead space(s)*", "*recirculation zone(s)*" or more commonly "*vortex (vortices)*". From a fundamental point of view, the secondary flows are very complex and not yet fully understood rheological phenomenon, representing one of the biggest challenges for both experimental and theoretical rheologists [15]. At the same time, this poses a serious problem in terms of processing, because the residence time of the material circulating in the secondary flow can be very long and, as a result, the polymer melt can be thermally degraded. In this case, the "black spots" flow irregularly away from the die and then create visible defects on the final surface of the extruded product [16].

Our comprehensive review paper [15], published in 2019, written in a historical perspective summarizes key factors (Newtonian viscosity, shear thinning, viscoelasticity, flow geometry, and extensional viscosity) influencing secondary entry flows for polymer melts and provides in-depth and critical discussion of the most important experimental and theoretical works on this subject. In addition, the timeliness of this interesting rheological topic can be demonstrated by following selected works published in the last five years. In 2017, Shahbani-Zahiri et al. published theoretical work [17] focused on the effects of recirculation regions and vortex

lengths on temperature distribution, Nusselt numbers and first/second normal stress differences in flows of non-isothermal viscoelastic fluids within a 1:3 sudden planar symmetric expansion channel. In the same year, López-Aguilar et al. [18] theoretically studied pressure drops in vortex contraction flows for Boger fluids described by continuous-spectrum and discrete-mode differential models. Two years later, Wang et al. [19] numerically investigated the sizes of recirculation regions during a flow bifurcation study in a symmetric planar contraction channel. In the same year, Tomcovic et al. [20] theoretically investigated the effects of ionic and hydrogen bonds on vortices in the entry flow region when extruding ionomers and their copolymers using of Kaye, Bernstein, Kearsley, and Zapas (K-BKZ) constitutive equation. Then, Hidema et al. [21] experimentally analysed the effects of solvent, solution concentration and channel geometry on the elastic corner vortex growth during the contraction/expansion channel flow of sodium hyaluronate (hyaluronic acid sodium salt, Na-HA) solution. In 2020, Sasmal [22], during his extensive numerical investigation of the flow characteristics of a wormlike micellar solution through long micropore with stepwise expansion and contraction, found a dependence of flow regimes with/without re-entrant/rear corner vortex flows on Weissenberg number and a nonlinear parameter representing scission energy required to break a long chain of micelle into two shorter chains. Further, Tseng [23] performed simulations of 3D contraction flows using the generalized Newtonian fluids (via the eXtended GNF-X model) over a wide range of Deborah numbers. In the same year, based on the analysis of the die swell behaviour of the extrudates, Farahanchi et al. [24] proposed a simple numerical approach to the quantitative prediction of the intensity of the corner vortices in the entry flow. Hereafter, Ferrás et al. [25] published another numerical study focused on Newtonian and viscoelastic (described by the Phan-Thien-Tanner constitutive equation) creeping flows through 1:4 planar expansion geometry considering the effect of slip boundary conditions and vortices. Thereinafter, in January 2021, Li et al. [26] developed a 2D depth-averaged inertial flow model for Newtonian fluids, which they subsequently tested by comparing the onset and size of vortex in sudden

contraction-expansion microchannels of varying lengths determined experimentally and theoretically in other studies. Further, in February 2021, Wu et al. [27] presented more fundamental experimental work investigating secondary entry flows in planar constriction microchannel under a wide range of Reynolds and Weissenberg numbers covering different polymer types (polyethylene oxide, polyvinylpyrrolidone and hyaluronic acid), molecular weights and concentrations. Another actual experimental work focused on corner vortices published in July 2021 by Raihan et al. [28] presents the study of five types of non-Newtonian fluids with distinct rheological properties and water flowing through a planar single-cavity microchannel over a wide range of Reynolds and Weissenberg numbers. In July 2021, Carlson et al. [29], published another interesting experimental study of 3D dilute polymer solution flow in the microfabricated glass square-square contraction geometry utilizing microtomographic particle image velocimetry to investigate viscoelastic instabilities including corner vortices. Very recently, in August 2021, Zargartalebi et al. [30] presented a systematic steady-state simulation of viscoelastic fluid at low Reynolds numbers through a channel with successive smooth contractions and expansions, with specific attention to vortex patterns that develop after contraction. Finally, in September 2021, Nodoushan et al. [31] published micro-particle image velocimetry study of yield stress and shear banding effects on the fluidic behaviours of cetyltrimethylammonium bromide/sodium salicylate wormlike micellar solutions flowing through 8:1 microfluidic planar contraction geometry. As can be seen, the phenomenon of secondary entry flow plays an important role in studies focused on the effects of molecular bonding [20] and molecular structure [21,27,28,31], development and testing of constitutive equations [18,23,25,26], parametric analysis [22,24,30], numerical algorithms [17,19] or experimental visualization methodology [29].

Despite the fact that the secondary flow in polymer melts extrusion is an interesting unstable rheological phenomenon with practical implications, its experimental investigation is an extremely challenging task because it is always hidden inside the extrusion die. The only way

to study it experimentally is to directly visualize the die entry region. However, this requires special optical experimental set up along with the proper software to evaluate the optical data. As follows from our recently published comprehensive review paper [15], secondary flow phenomenon has been mainly experimentally studied by velocity field visualization techniques, i.e. particle tracking velocimetry [32-40] or laser-Doppler velocimetry [16,41-45]. Although these techniques are sufficiently accurate for this purpose, they have several critical disadvantages. First, micro-sized inorganic particles (usually glass beads or TiO_2) added in ppm level into investigated polymer melt to track individual streamlines may slightly deform the studied velocity field. Second, velocity visualization is very time consuming, especially in the case of laser-Doppler velocimetry (LDV) operating with high spatial and temporal resolution. This can subsequently lead to thermal degradation (i.e. significant change of rheological properties) in the case of thermally-sensitive polymer melts. Third, the LDV technique works on a mesh instead of a natural streamline base (streamlines are calculated from raw data during their software postprocessing). Finally, the phenomenon of secondary entry flow that occurs during the extrusion of polymer melts is definitely stress-driven mechanism, and therefore a stress field rather than a velocity flow field should be preferred for better fundamental understanding.

In order to overcome the above-mentioned disadvantages, the flow induced birefringence (FIB) technique has been used in several preliminary experimental research works [33,46,47]. However, in none of these works was the fundamental question "Are the secondary entry flow inner boundary evaluated from velocity and stress flow fields the same?" clearly answered. Therefore, we prepared this experimental work, in which we first present a detailed analysis of the secondary entry flow inner boundary for LDPE melt evaluated through velocity (particle tracking) and stress (FIB) fields, secondly, we show the effect of flow conditions (specifically shear rate and temperature) using the FIB method and finally compare these data with the available LDV data for the same polymer melt and comparable flow conditions.

EXPERIMENTAL

The experimental part is divided into the following steps. First, a well-rheologically characterized LDPE polymer melt was selected. Then, the secondary entry flow inner boundary under suitable flow conditions was simultaneously analysed by particle tracking (i.e., velocity flow field visualization technique) and FIB (i.e. stress flow field visualization technique). Based on this step, a simple methodology for evaluating the size (area) of secondary entry flow was proposed and subsequently used to study the effects of flow conditions. Finally, these data were compared with the LDV data available in the open literature for the same polymer melt and comparable flow conditions.

Material

In this work, LDPE Lupolen 1840H polymer melt was selected. This polymer is in principle very similar (but not identical) to Lupolen 1810H or the IUPAC A melts [44], and it is well rheologically characterized in many previous research works, from which we have selected over the most important characteristics (see Fig. 1 and Tab. 1). This LDPE was originally produced in Ludwigshafen (Germany) by BASF (now Lyondell Basell) by radical polymerization in a high-pressure tubular reactor and therefore, it has a randomly long-chain branched structure [49,51].

Secondary Entry Flow(s) Visualization

In this chapter, basic principles of flow induced birefringence and particle tracking velocimetry techniques are briefly introduced, and then the experimental setup together with the chosen flow conditions used in our tests are presented in more detail.

Flow Induced Birefringence

As follows from the basic flow induced birefringence theory [52-56], under no-flow conditions, amorphous polymer melts are optically isotropic. However, in flow, stress as

internal material reaction to the external force/pressure/displacement action causes distortion and orientation of polymer chains, which leads to optical anisotropy. As a result of this anisotropy, the refractive indices in the flowing polymer melt change locally. In order to visualize the local stress field within the flow domain, the following basic plane polariscope principle must be used. A polariser (an optical filter passing light of a certain polarisation and blocking waves of another polarisation) converts monochromatic light into a polarised plane. As this light passes through the optically oriented polymer melt, it refracts into two plane polarised components, known as ordinary and extraordinary waves. Each of these waves has a different velocity based on the refractive index of the melt encountered during its transmittance. In this way, the flowing polymer melt is optically biaxial, having three different, mutually perpendicular principal axes with three different principal refractive indices. One of these axes is identical to the plane of polarised light and the other two lie in the observation plane. The flow field is then light or dark (dark bands are generally known as *isoclinic fringes*) depending on whether or not the orientation of the polarised light matches the orientation of the two principal axes. Finally, the analyser divides the components of the polarised light into one plane, and therefore the temporary double reflection (birefringent) effect caused by the stress-caused orientation in polymer melt can be measured from the resulting interference waves.

In this work, a circular polarization formed by two quarter-wave plates placed between the polariser/analyser on each side of the flow cell was used. In this case, dark bands represent the loci of points along which the difference in the first and second principal stress remains the same and are generally known as *isochromatic fringes*. Each *isochromatic fringe* represents a certain level of total stress conditions (i.e. combined shear and normal stresses). Then, the *isochromatic fringe* pattern visualizes the total stress (principle stress difference) flow field.

The initial calibration of this technique was performed in the following steps. First, the optical bench was moved in all three dimensions to find the correct position in which the flow geometry was placed exactly on the main optical axis (i.e. directly between the light, the optical

filters, and the camera). Second, the polarization planes of the individual optical filters were set as follows – analyser 0°, first quarter wave plate (between analyser and visualization cell) 315°, second quarter wave plate (between visualization cell and polarizer) 45° and polarizer 90°. Third, a 15 mm long extension tube was placed on the lens to adjust the camera focus. Finally, the maximum mass flow rates under the selected processing conditions were determined as the onset of the well-known melt fracture phenomenon.

Particle Tracking Velocimetry

The particle tracking velocimetry (PTV) technique, which is used to visualize velocity flow fields, is generally based on adding small amounts of inorganic particles (usually micro-sized glass beads or titanium dioxide) as flow tracers to the extruder hopper and mixing with bulk polymer to provide isokinetic seeding of the flow. Gels or dust particles having a typical size of hundredths or thousandths of millimetres, typically present in commercially available polymers, have also been used for this purpose [57]. These particles make it possible to track and visualize each individual streamline in the liquid. This method is usually performed as a so-called streak photography technique using the transparent die geometry, which can be equipped with a so-called "laser-sheet" perpendicular to the camera in order to visualize individual streamlines inside the visualization cell. The flow of the polymer melt with small particles is then captured at a given exposure time varying according to the flow rate. Afterwards, higher velocity streamline has longer particle trace. However, the main disadvantage of this method is the low spatial and temporal resolution, because with increasing flow rate, the exposure time must be extremely shortened in order to maintain position accuracy. This leads to low light at the shortest exposure times, which can be partially overcome by using a camera to capture visualization experiments in the form of a film instead of making individual streak photographs.

In this work, we used the particle tracking method originally described by den Otter [57] using small gels/dust particles naturally present in every grade of the commercially available polymer. In this way, we have eliminated possible streamline distortions when visualizing the velocity field that could occur when using artificial inorganic particles. PTV data extraction was performed as follows. After each individual test, the analogue recording was converted to digital one using a BT848 based PC-TV card. Then, last PTV image of the recording (after stabilization of the flow conditions, i.e. typically after 15 minutes) was extracted in commercially available Windows Movie Maker software. Finally, based on the known dimensions of the extrusion die and the camera resolution, all images taken from the movie were dimensionally calibrated in Didger^{TM} software (Golden Software LLC, USA) using four calibration points (corners of each image). The performed calibration made it possible to relate the position expressed in pixels to the position expressed in the Cartesian coordinate system in millimetres in order to obtain each individual position of a given particle and the secondary flow boundary for each individual processing condition.

Experimental Set-up

An overall 3D view of the experimental flow visualization extrusion set-up is shown in Fig. 2. It consists of a computer-controlled single screw extruder *Betol BK38* (Davis-Standard, UK) with a screw diameter of 38 mm and a length of 30D (operating at a screw speed of up to 100 rpm) electrically heated by four zones and following special accessories. First, an optical bench moveable in all three dimensions (see Fig. 3) consists (from right to left) of a mercury vapour lamp with a wavelength λ = 546 nm as a of green light source, a polariser plate, two quarter wave plates (between them a flow visualization cell is placed), an analyser plate (all from *Edmund Optics*), a colour filter and an analogue CCD video camera (*Pulnix PEC 3010* model with a resolution of 720x576 pixels) equipped with a Nikon lens and a 15 mm long extension tube. Second, a flow visualization cell (see partial section view in Fig. 4) made as a universal

slit die with strain-free borosilicate glass windows placed on both sides of the flow visualization cell allows monitoring of the polymer melt flow behaviour in the die entry region. The visualization die was carefully designed (see Fig. 4) with respect to possible flow fields deviations due to the inhomogeneous temperature profile inside the die, especially near the glass walls of the die. In general, small temperature changes in the visualization cell could dramatically disrupt the symmetry of the resulting velocity profile, especially with respect to the LDPE polymer melt as a material with high flow activation energy. The corresponding research was conducted by Schmidt et al. during their accurate laser-Doppler velocimetry measurement of comparable LDPE in a similar visualization cell, but with only one glass sidewall [41]. Based on their accurate velocity profile measurements and taking into account all their experimental limitations, including particularly unheated glass window and the possible slip on the glass wall, they concluded that the symmetry of the measured velocity profiles in both flow planes is satisfactory and thus demonstrates that the temperature distribution in the die is good enough for reliable measurements. The die is further equipped with a 1,500 PSI (10.3421 MPa) pressure transducer with a sampling rate of 15 per second and a rectangular slit flow geometry consisting of two replaceable inside-die steel inserts. The dimensions of these inserts were carefully chosen with respect to eliminating possible 3D side effects in the studied birefringence flow fields. As follows from the theoretical and experimental study presented by Clemeur et al. [58] the effect of 3D side effects is significant for *aspect ratios* (i.e. slit width to gap ratios) below 10. Therefore, we used a flow geometry with dimensions of the upstream channel depth H = 15 mm, width W = 10 mm, slit gap G = 0.938 mm, and slit length L = 15 mm (see schematic view of die inserts in Fig. 5). Thus, our aspect ratio (AR) was 10.7 and contraction ratio (CR) was 16. Finally, a video recorder was used to capture experimental optical birefringence tests on analogue tape (25 frames per second).

Flow Conditions

Experimental investigation was carried out under following flow conditions. In order to eliminate possible thermal degradation of the investigated polymer melt, the extruder zones were heated to temperatures (from hopper to die): T_1 = 150°C, T_2 = 160°C, T_3 = 160°C and T_4 = 160°C, respectively. The two transition sections between the extruder and the flow visualization cell as well as the flow visualization cell were stepwise heated on 135°C, 130°C (die temperature of 130°C), 150°C, 150°C (die temperature of 150°C), 162°C, 170°C (die temperature of 170°C) and 170°C, 190°C (die temperature of 190°C), respectively. Flow visualization experiments were performed at various mass flow rates ranging from 0.04 $kg.hr^{-1}$ to 1.9 $kg.hr^{-1}$ (i.e., from 17 s^{-1} to 390 s^{-1} for the downstream apparent shear rates $\dot{\gamma}_{APP.}$). These rates varied according to the temperature examined, and the maximum $\dot{\gamma}_{APP}$ was chosen just below the occurrence of the well-known melt fracture instability.

Results and Discussion

The experimental results and their discussion include the following three main parts. First, the inner boundary of the secondary entry flow evaluated from the velocity (particle tracking method) and stress fields (flow induced birefringence method) is carefully analysed. Secondly, based on this analysis, a simple method for determining the size (area) of the secondary entry flows is proposed and subsequently used to study the effects of temperature and downstream apparent shear rate. Finally, the presented data are compared with the laser Doppler velocimetry data available in the open literature for the same polymer melt and similar processing conditions.

Evaluation of Secondary Entry Flow Using Flow Induced Birefringence

As indicated in the preliminary research work of Boukellal et al. [46], a stress visualization technique based on flow induced birefringence could be a useful technique to determine the

area of the secondary entry flow for polymer melts. However, a detailed analysis of the inner boundary of the entry flow to support this hypothesis has not been performed. Therefore, in our work, the position of this boundary determined simultaneously by the stress and velocity flow fields was carefully analysed. As the first it was evaluated from the FIB image, while as the second it was visualized by particle tracking using the technique of den Otter et al. [57]. This technique makes it possible to eliminate possible streamline distortion during velocity field visualization by using the very small gels/dust particles naturally present in every grade of the commercially available polymer instead of adding artificial inorganic particles.

A comparison of the secondary entry flow boundary determined from velocity and stress fields was performed at a temperature of 190°C and downstream apparent shear rate of $182s^{-1}$. Fig. 6 shows the analysis of four streamlines in different positions across the die tracked from the movie at different times (in steady-state regime – see following text). The right side shows the actual FIB image with the four tracked particles. As can be seen, the stress flow field shows a typical funnel-shaped pattern with many isochromatic fringes near the centreplane along with a fringe-free corner region (multimedia view). The following four streamlines were selected for tracking – *streamline 1* near the centreplane, *streamline 2* in the continually stretched region, and *streamlines 3/4* coming twice/once through secondary flow, respectively. Each individual position of a given particle was digitized in Didger™ software after careful calibration of the image dimensions. It can be clearly seen that the inner boundary of the secondary entry flow indicated by the *streamlines 3* and *4* lies at the boundary fringe between the funnel-shaped fringes and the fringe-free corner region. It is important to note that in our experimental setup, monochromatic light passes through the entire die, and therefore, the FIB image represents the integral values of the isochromatic stress fringes. However, as mentioned earlier in the text, possible 3D side effects were eliminated with the correct selected aspect ratio (*AR*) of the die, which is higher than 10. In addition, with regard to particle tracking, the optical setup used was

focused at the right side of the die wall (in the extrusion direction), and therefore only particles in this region are visible.

In the next step, the movement of the particle along *streamline 4* entering the die at position x = -6.90 mm and z = 12.85 mm (i.e. very close to the side wall of the die, and thus representing well the inner boundary of the secondary entry flow) was carefully analysed as follows. First, the velocity (Fig. 7) and the extensional strain rate (Fig. 8) both along the *streamline 4* were plotted as a function of the non-dimensional streamline distance (i.e., each particular streamline length at a given particle position divided by the full streamline length). As can be seen, both graphs show two maxima – the first represents the entry of the particle into the secondary flow and the second shows the exit of the particle from the secondary flow and its subsequent entrance to the slit. In both figures, the motion of the particle was divided into two main parts – the position where the particle slows down (i.e. it is compressed) and the position where the particle accelerates (i.e. it is stretched). In the case of *streamline 4*, where the particle shows only one rotation, these areas (shown as blue diamonds and red circles, respectively) well represent inner boundary of the secondary flow. In addition, the positions where the particle *enters* the secondary flow are drawn as closed symbols and the positions where the particle is *in* the secondary flow and *leaves* it are drawn as open symbols. Based on this motion analysis, the inner boundary of the secondary flow was constructed and compared in Fig. 9 with the FIB image. As can be clearly seen, the inner boundary actually lies at the boundary fringe between the funnel-shaped fringes and the fringe-free corner region. Thus, it can be assumed that the boundaries of the secondary flow evaluated from velocity and stress fields are very close to each other, and therefore in the next part of this work the sizes of the secondary entry flow were evaluated as their areas calculated from FIB images taken during individual tests at selected processing conditions.

Finally, the test conditions were carefully evaluated. The pressures and secondary flow areas (calculated according to the method described above) for minimum ($17s^{-1}$ at 150°C) and

maximum ($390s^{-1}$ at 190°C) downstream apparent shear rates were plotted as a function of testing time – see Figs. 10 and 11, respectively. At low shear rates, no overshoots in the pressure and secondary flow area were detected (see Fig. 10), but at high shear rates, significant overshoots were present in both variables (see Fig. 11). In both cases, the pressures and areas of the secondary flow areas did not pulsate, indicating that the melting in the extruder during the tests was uniform. In addition, in both cases, the 15-minute testing time was long enough to reach steady-state, and therefore the FIB images were taken after this time to calculate the secondary flow areas at given processing conditions.

In the last part of this work, the effects of temperature and the downstream apparent shear rate were carefully studied by the proposed methodology. The obtained results were compared with the corresponding data obtained by LDV for comparable flow conditions taken from the open literature [16].

Effect of Temperature on Secondary Flow Size

The effect of temperature on the secondary flow size can be seen in Figs. 12 and 13. In the Fig. 12, the right sides show the actual FIB images, while the left sides represent the digitized inner boundaries of the secondary flow at the same downstream apparent shear rate ($30s^{-1}$) and four different temperatures (130°C, 150°C, 170°C and 190°C). As can be seen, the area of the secondary flow first increases, reaches a maximum at 150°C and then decreases rapidly. This trend is more visible in Fig. 13, where the area of the secondary flow plotted against temperature for three different downstream apparent shear rates shows a typical non-monotonic dependence in which the maximum is slightly shifted upwards at higher temperatures. This trend correlates well with earlier works published by Schwetz et al. [44] who explained this by the non-monotonic dependence of the viscosity (or Trouton) ratio (i.e. uniaxial extensional viscosity divided by three-times the shear viscosity). This revolutionary idea was firstly introduced by White and Baird in 1988 in their experimental [33] and theoretical [59] papers, representing the first comprehensive attempt to gain a fundamental understanding of the

secondary entry flow nature in polymer melts. Based on their die entry flow results for LDPE and PS polymer melts, they concluded that "It appears that the ratio of extensional stress to shear stress…determines the presence or absence of vortex growth…It was found that the value of this ratio was over twice as high for LDPE, which exhibited vortex growth, than for PS which did not…but it is not understood why… extensional stress …ratio with the shear stress should be significant…In fact it is believed that it is the strain rate and strain rate hardening of the fluid which leads to the formation of an entry angle and it is the early onset of shear thinning at low shear rates which allows momentum to be transferred into the corners and hence create recirculation flow" [33]. A similar but more detailed study using laser-Doppler velocimetry was performed by Schwetz et al. [44], who first convincingly showed that the Trouton ratio very good correlates with the area of the secondary flow plotted against the temperature or against a representative elongational rate. This representative elongational rate was obtained assuming that the maxima in the secondary flow area and the Trouton ratio are interrelated and form complicated flow behaviour of melts in die entry region. The fact that "…elongational viscosity and vortex size as a function of temperature or apparent shear rate, respectively, can be related to each other" represents "…heuristic evidence for a relationship between elongational behavior and secondary flow. These relationships are somewhat surprising as they are found by introducing an empirically determined representative elongational rate" [44].

Fig. 14 shows a direct comparison of the secondary entry flow areas from stress fields (flow-induced birefringence) and velocity fields (laser-Doppler velocimetry). LDV comparative data are taken from an experimental study published by Hertel and Münstedt [16]. They used the same polymer melt, comparable visualization cell design (both equipped by glass wall), similar contraction ratios – 14 (LDV study) and 16 (FIB study) and aspect ratios of die entry region – 14 (LDV) and 10.7 (FIB), apparent shear rates – 70 s^{-1} (LDV) and 92 s^{-1} (FIB) and

temperatures – 135°C, 150°C, 165°C, 180°C, 200°C and 220°C (LDV) and 150°C, 170°C and 190°C (FIB). As can be clearly seen, both data sets correlate very well.

Effect of Downstream Apparent Shear Rate on Secondary Flow Size

The effect of the downstream apparent shear rate on the size of the secondary flow was performed in a similar manner as in the previous case. Fig. 15 shows a comparison between the actual FIB image (right side) and the digitized inner boundary line of the secondary flow (left side) at one temperature (150°C) and four different downstream apparent shear rates ($17s^{-1}$, $30s^{-1}$, $62s^{-1}$ and $92s^{-1}$). Similar to the temperature effect, also dependent on the shear rate, the secondary flow area shows a typical non-monotonic trend, which is clearer in Fig. 16 for three different temperatures (150°C, 170°C and 190°C). In this case, the maximum in a given dependence is shifted downwards at higher shear rates. This trend can be simply explained by the temperature dependence of the Trouton ratio on the apparent shear rates, where the same trend (i.e. shift of the maximum at higher temperature and apparent shear rate downwards) is generally valid [48, 60] and again correlates well with earlier conclusions published by Hertel at el. [44]. Finally, a direct comparison with laser-Doppler velocimetry-based data taken from the same study [16] as in the previous section on temperature effects is shown in Fig. 17 for 165°C (LDV method) and 170°C (FIB method). As in the temperature dependence, a reasonably good agreement was obtained between these two data sets, which supports the idea that the inner secondary flow boundaries evaluated by the two methods are very close.

CONCLUSION

As has been experimentally shown, the inner secondary flow boundary evaluated by velocity-based (i.e. by particle tracking) and stress-based (i.e. by flow induced birefringence) methods are very close. Based on this fact, a new methodology for evaluating the secondary flow area to study the effects of different flow conditions was proposed and used. Despite to

conventional flow field visualization methods (particle tracking or laser-Doppler velocimetry), the proposed FIB method is very fast (one test lasted only 15 minutes), sufficiently accurate (compared to LDV data) and in addition no artificial inorganic particles that can deform the studied flow field must be added. Secondary entry flow areas plotted as a function of temperature and apparent shear rate studied by this method show typical non-monotonic trends going through one maximum. The presented FIB data in comparison with LDV data taken from the open literature for the same polymer melt and comparable flow conditions shows a very good agreement. This strongly supports the idea that the inner boundary of the secondary flow evaluated from the velocity and stress fields are very close. This work could therefore pave the way for further stress-induced birefringence studies, which are extremely necessary for a deeper fundamental understanding of the interesting secondary entry flow phenomenon.

DATA AVAILABILITY

The data that supports the findings of this study are available within the article and its supplementary material.

SUPPLEMENTARY MATERIAL

See the supplementary material for the STEP files containing the three-dimensional data related to the experimental flow visualization setup shown in Figures 2 - 4.

ACKNOWLEDGMENTS

The authors wish to acknowledge the Grant Agency of the Czech Republic (grant No. 21-09174S) for the financial support. Moreover, authors thank Phil Coates, Tim Gough, Mike Martyn, Steve Brook, Ian Smith and Roy Dixon from University of Bradford for allowing us to perform all flow visualization experiments on University of Bradford (UK) laboratory equipment as well as for their support.

APPENDIX

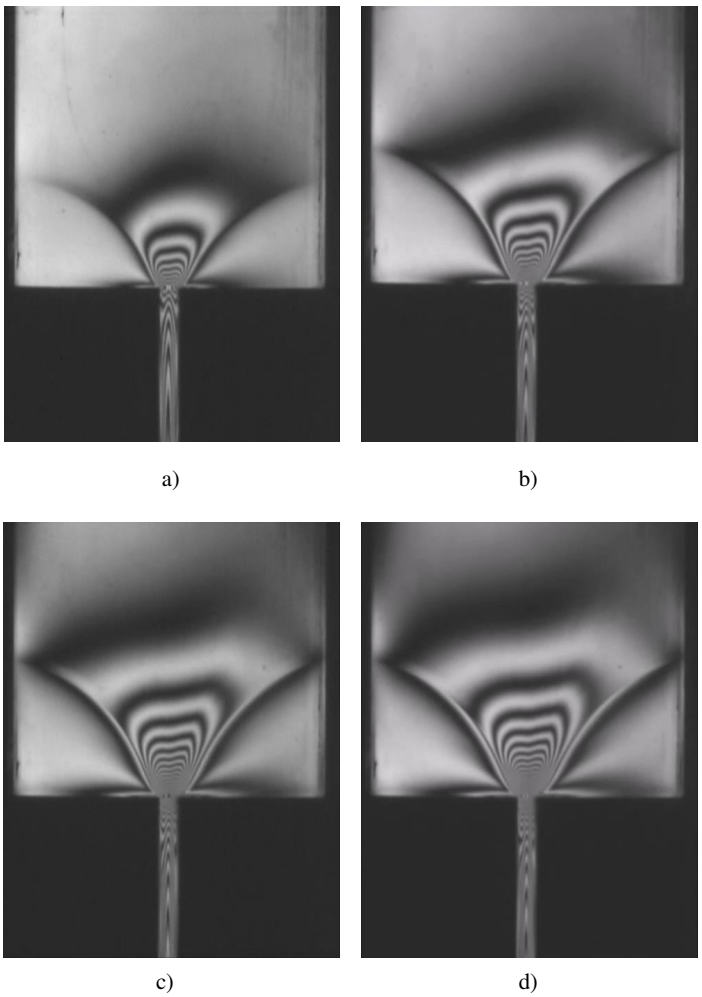

Figure 18: Flow-induced birefringence images for apparent shear rate a) $10s^{-1}$ (multimedia view), b) $17s^{-1}$ (multimedia view), c) $23s^{-1}$ (multimedia view) and d) $30s^{-1}$ (multimedia view) at 130°C taken after 15-minute test.

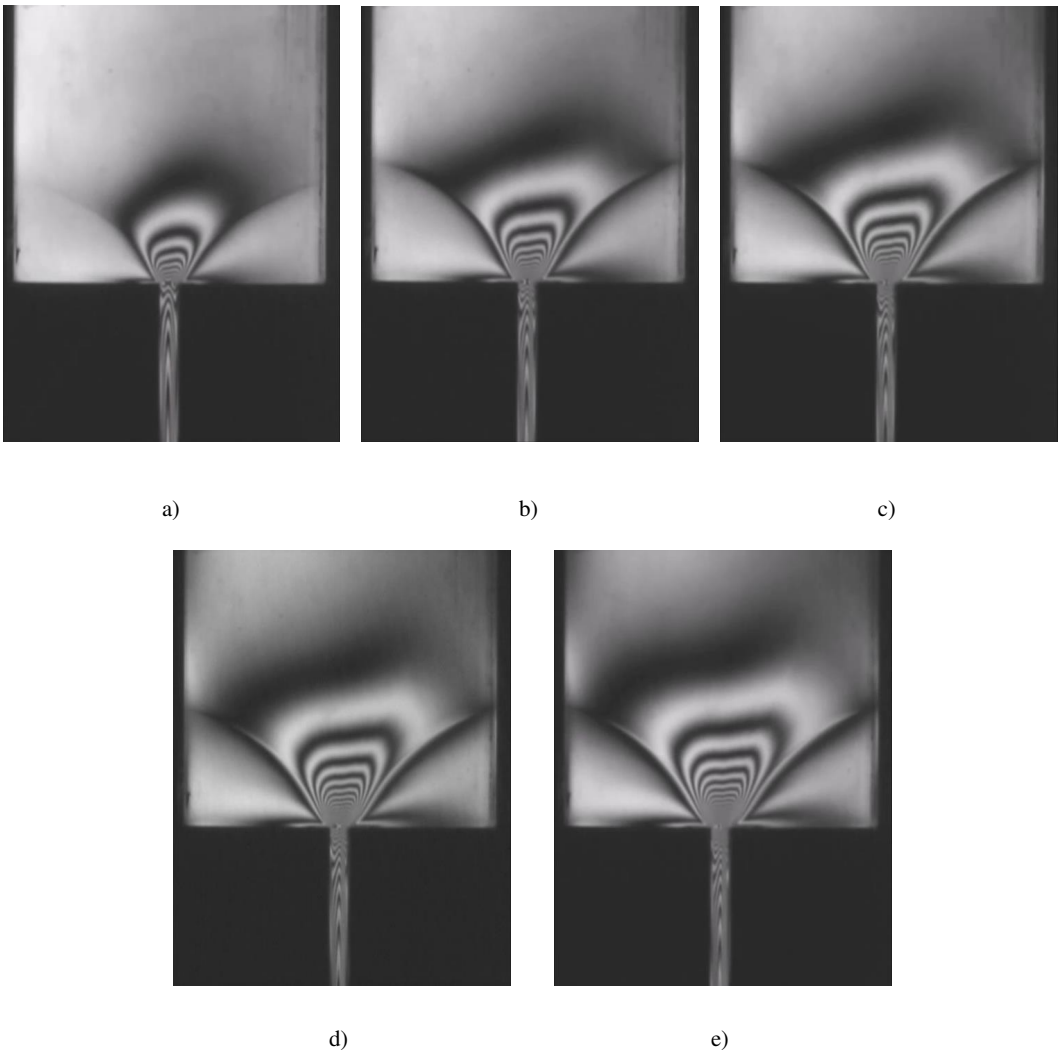

Figure 19: Flow-induced birefringence images for apparent shear rate a) 17s^{-1} (multimedia view), b) 30s^{-1} (multimedia view), c) 62s^{-1} (multimedia view), d) 75 s^{-1} (multimedia view) and e) 92 s^{-1} (multimedia view) at 150°C taken after 15-minute test.

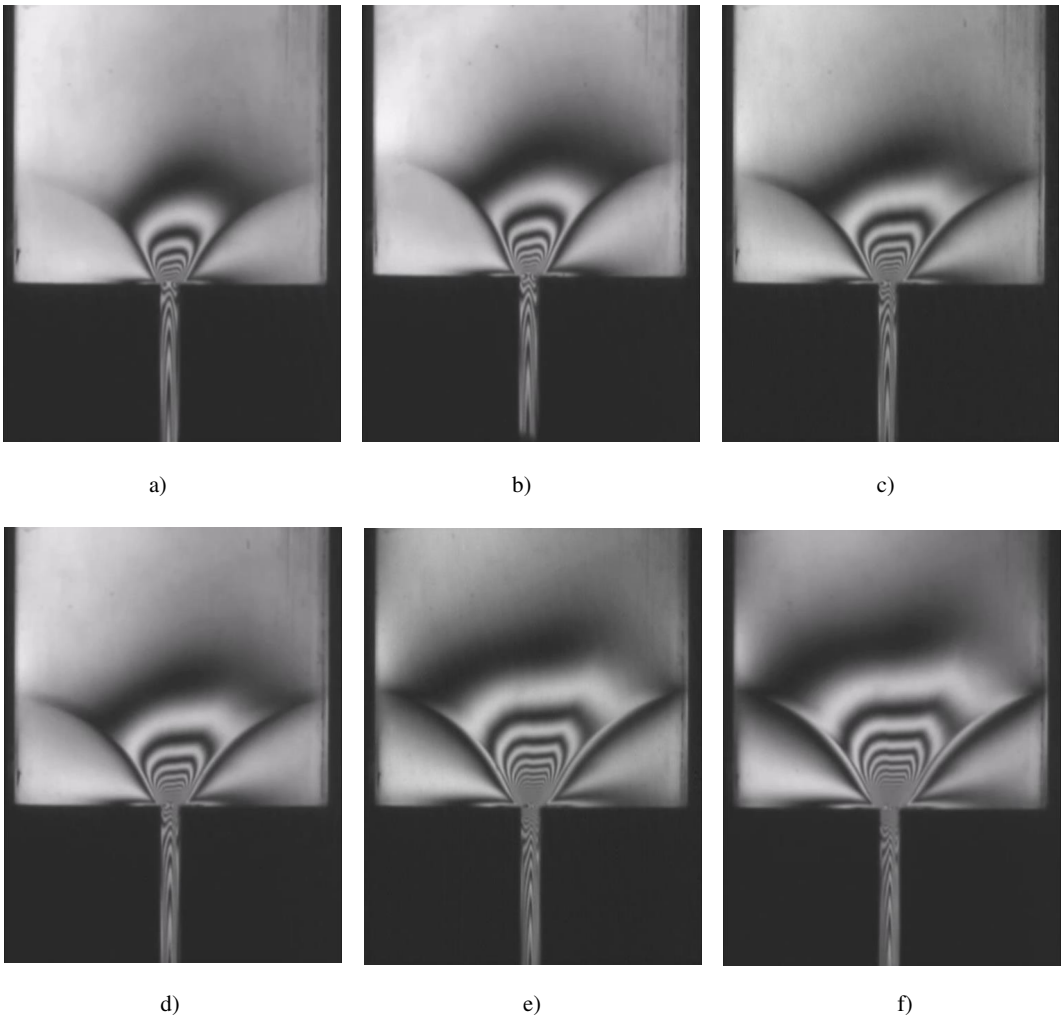

Figure 20: Flow-induced birefringence images for apparent shear rate a) 17s^{-1} (multimedia view), b) 30s^{-1} (multimedia view), c) 75s^{-1} (multimedia view), d) 92 s^{-1} (multimedia view), e) 150 s^{-1}(multimedia view) and f) 182 s^{-1} (multimedia view) at 170°C taken after 15-minute test.

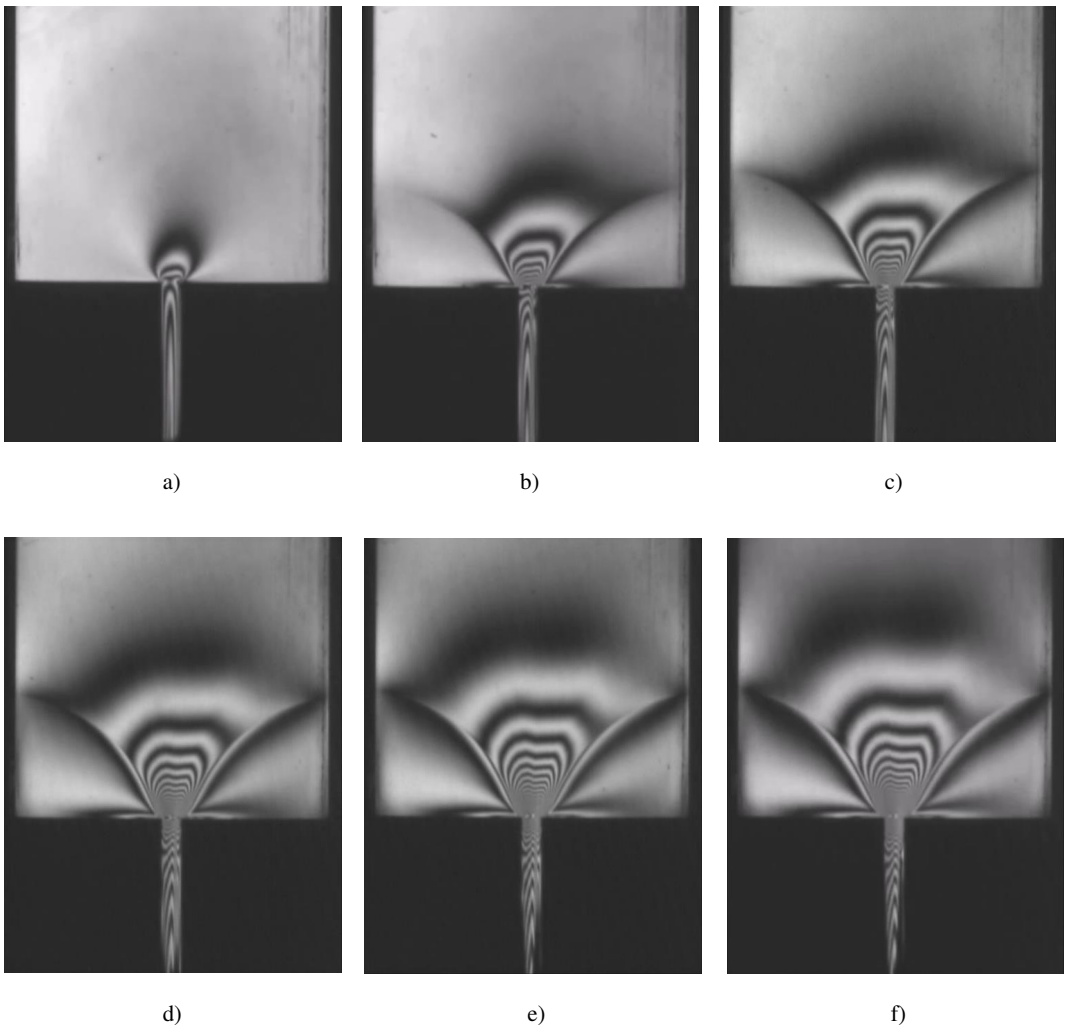

Figure 21: Flow-induced birefringence images for apparent shear rate a) 30s^{-1} (multimedia view), b) 92s^{-1} (multimedia view), c) 182s^{-1} (multimedia view), d) 220 s^{-1} (multimedia view), e) 300 s^{-1}(multimedia view) and f) 390 s^{-1} (multimedia view) at 190°C taken after 15-minute test.

REFERENCES

1. Leonov, A. I. Prokunin, A., Nonlinear Phenomena in Flows of Viscoelastic Polymer Fluids (Springer Science & Business Media, 2012).
2. Baird, D. G., Collias, D. I. Polymer Processing: Principles and Design (John Wiley & Sons, 2014).
3. Carroll, C. P. Joo, Y. L., Axisymmetric Instabilities in Electrospinning of Highly Conducting, Viscoelastic Polymer Solutions, *Phys. Fluids* **21**, 103101 (2009).
4. Zuliki, M., Zhang, S., Tomcovic, T., Hatzikiriakos, S.G., Capillary Flow of Sodium and Zinc Ionomers, *Phys. Fluids* **32**, 023106 (2020).
5. Bodnar, T., Sequeira, A., Prosi, M., On the Shear-Thinning and Viscoelastic Effects of Blood Flow under Various Flow Rates, *Appl. Math. Comput*. **217**, 5055-5067 (2011).
6. Elhanafy, A., Guaily, A. Elsaid, A., Numerical Simulation of Blood Flow in Abdominal Aortic Aneurysms: Effects of Blood Shear-Thinning and Viscelastic Properties, *Math Comput Simul.* **160**, 55-71 (2019).
7. Ali, N., Hussain, S. Ullah, K., Theoretical Analysis of Two-Layered Electro-osmotic Peristaltic Flow of FENE-P Fluid in an Axisymmetric Tube, *Phys. Fluids* **32**, 023105 (2020).
8. Galindo-Rosales, F. J., Campo-Deano, L., Pinho, F. T., Van Bokhorst, E., Hamersma, P. J., Oliveira, M. S. N., Alves, M. A., Microfluidic Systems for the Analysis of the Viscoelastic Fluid Flow Phenomena in Porous Media, *Microfluid. Nanofluid*. **12**, 485-498 (2012).
9. James, D. F., McLaren, D. R., The Laminar Flow of Dilute Polymer Solutions through Porous Media, *J. Fluid Mech*. **70**, 733-752 (1975).
10. Li, X., Sarsenbekuly, B., Yang, H., Huang, Z., Jiang, H., Kang, X., Li, M., Kang, W., Luo, P., Rheological Behaviour of a Wormlike Micelle and an Amphiphilic Polymer Combination for Enhanced Oil Recovery, *Phys. Fluids* **32**, 073105 (2020).

11. Park, S. W., Analytical Modeling of Viscoelastic Dampers for Structural and Vibrational Control, *Int. J. Solids Struct*. **38**, 8065-8092 (2001).
12. Makris, N., Dargush, G. F., Constantinou, M. C., Dynamic Analysis of Viscoelastic-Fluid Dampers, *J. Eng. Mech*. **121**, 1114-1121 (1995).
13. Syrakos, A., Dimakopoulos, Y., Tsamopoulos, J., Theoretical Study of the Flow in a Fluid Damper Containing High Viscosity Silicone Oil: Effects of Shear-Thinning and Viscoelasticity, *Phys. Fluids* **30**, 030708 (2018).
14. Tordella, J. P., Capillary Flow of Molten Polyethylene - A Photographic Study of Melt Fracture, *Trans. Soc. Rheol.* **1**, 203-212 (1957).
15. Musil, J., Zatloukal, M., Historical Review of Secondary Entry Flows in Polymer Melt Extrusion, *Polym. Rev.* **59**, 338-390 (2019).
16. Hertel, D., Münstedt, H., Dependence of the Secondary Flow of a Low-Density Polyethylene on Processing Parameters as Investigated by laser-Doppler Velocimetry, *J. Non-Newtonian Fluid Mech.* **153**, 73-81 (2008).
17. Shahbani-Zahiri, A., Hassanzadeh, H., Shahmardan, M. M., Norouzi, M., Investigation of Pitchfork Bifurcation Phenomena Effects on Heat Transfer of Viscoelastic Flow Inside a Symmetric Sudden Expansion, *Phys. Fluids* **29**, 113101 (2017).
18. López-Aguilar, J. E., Webster, M. F., Tamaddon-Jahromi, H. R., Manero, O., Binding, D. M., Walters, K., On the Use of Continuous Spectrum and Discrete-Mode Differential Models to Predict Contraction-Flow Pressure Drops for Boger Fluids, *Phys. Fluids* **29**, 121613 (2017).
19. Wang, Y., Ferrer, E., Martínez-Cava, A., Zheng, Y., Valero, E., Enhanced Stability of Flows through Contraction Channels: Combining Shape Optimization and Linear Stability Analysis, *Phys. Fluids* **31**, 074109 (2019).

20. Tomcovic, T., Mitsoulis, E., Hatzikiriakos, S. G., Contraction Flow of Ionomers and Their Corresponding Copolymers: Ionic and Hydrogen Bonding Effects, *Phys. Fluids* **31**, 033102 (2019).
21. Hidema, R., Oka, T., Komoda, Y., Suzuki, H., Effects of Flexibility and Entanglement of Sodium Hyaluronate in Solutions on the Entry Flow in Micro Abrupt Contraction-Expansion Channels, *Phys. Fluids* **31**, 072005 (2019).
22. Sasmal, C., Flow of Wormlike Micellar Solutions through a Long Micropore with Step Expansion and Contraction, *Phys. Fluids* **32**, 013103 (2020).
23. Tseng, H.-C., A Revisitation of Generalized Newtonian Fluids, *J. Rheol.* **64**, 493-504 (2020).
24. Farahanchi, A., Azevedo, D., Czazasty, J., Effects of Viscoelastic Properties of Polymer Melts on the Entrance Vortex Flow, *Annual Technical Conference – ANTEC, Conference Proceedings*, **Vol. 1**, 94-98 (2020).
25. Ferrás, L. L., Afonso, A. M., Alves, M. A. et al., Newtonian and Viscoelastic Fluid Flows through an Abrupt 1:4 Expansion with Slip Boundary Conditions, *Phys. Fluids* **32**, 043103 (2020).
26. Li, D. et al., A Depth-Averaged Model for Newtonian Fluid Flows in Shallow Microchannels, *Phys. Fluids* **33**, 012002 (2021).
27. Wu, S., et al., Polymer Effects on Viscoelastic Fluid Flows in a Planar Constriction Microchannel, *J. Non-Newtonian Fluid Mech.* **290**, 104508 (2021).
28. Raihan, M. K. et al., Flow of Non-Newtonian Fluids in a Single-Cavity Microchannel, *Micromachines*, **12**, 836-855 (2021).
29. Carlson, D. W., Shen A. Q., Haward S. J., Microtomographic Particle Image Velocimetry Measurements of Viscoelastic Instabilities in a Three-Dimensional Microcontraction, *J. Fluid Mech.* **923**, R6 (2021).

30. Zargartalebi, A., Zargartalebi, M., Benneker, M., Analysis of Vortices in Viscoelastic Fluid Flow through Confined Geometries at Low Reynolds Numbers, *AIP Advances* **11**, 085213 (2021).

31. Nodoushan, E., J., Lee, Y. J., Lee, G.-H., Kim, N., Quasi-Static Secondary Flow Regions Formed by Microfluidic Contraction Flows of Wormlike Micellar Solutions, *Phys. Fluids* **33**, 093112 (2021).

32. White, S. A., Baird, D. G., The Importance of Extensional Flow Properties on Planar Entry Flow Patterns of Polymer Melts, *J. Non-Newtonian Fluid Mech*. **20**, 93-101 (1986).

33. White, S. A., Baird, D. G., Flow Visualization and Birefringence Studies on Planar Entry Flow Behavior of Polymer Melts, *J. Non-Newtonian Fluid Mech.* **29**, 245-267 (1988).

34. Tremblay, B., Visualization of the Flow of Linear Low Density Polyethylene/Low Density Polyethylene Blends through Sudden Contractions, *J. Non-Newtonian Fluid Mech*. **43**, 1-29 (1992).

35. Tremblay, B., Visualization of the Flow of Low Density Polyethylene/Polystyrene Blends through a Planar Step Contraction, *J. Non-Newtonian Fluid Mech.* **52**, 323-331 (1994).

36. Coates, P. D., Matsuoka, M., Kamala, M., Martyn, M., Observation of 3-D Effects in Flow Visualization of Polymer Melts, *57th Annual Technical Conference (ANTEC),* New York **1**, 1167-1171 (1999).

37. Coates, P. D., Matsuoka, M., Kamala, M., Martyn, M., Observation and Quantification of 3D Effects in Polymer Melt Entry Flows, *15th Annual Meeting of Polymer Processing Society*, Hertogenbosch, The Netherlands (1999).

38. Gough, T., Spares, R., Kelly, A. L., Brook, S. M., Coates, P. D., Three-Dimensional Characterisation of Full Field Stress and Velocity Fields for Polyethylene Melt through Abrupt Contraction, *Plastics, Rubber and Composites* **37**, 158-165 (2008).

39. Kazatchov, I. G., Yip, F., Hatzikiriakos, S. G., The Effect of Boron Nitride on the Rheology and Processing of Polyolefines, *Rheol. Acta* **39**, 583-594 (2000).

40. Mitsoulis, E., Kazatchov, I. B., Hatzikiriakos, S. G., The Effect of Slip in the Flow of a Branched PP Melt: Experiments and Simulations, *Rheol. Acta* **44**, 418-426 (2005).

41. Schmidt, M., Wassner, E., Münstedt, H., Setup and Test of a Laser Doppler Velocimeter for Investigations of Flow Behaviour of Polymer Melts, *Mech. Time-Depend. Mat.* **3**, 371-393 (1999).

42. Wassner, E., Schmidt, M., Münstedt, H., Entry Flow of a Low-Density-Polyethylene Melt into a Die: An Experimental Study by Laser-Doppler Velocimetry, *J. Rheol.* **43**, 1339-1353 (1999).

43. Münstedt, H., Schwetz, M., Heindl, M., Schmidt, M., Influence of Molecular Structure on Secondary Flow of Polyolefin Melts as Investigated by a Laser-Doppler Velocimetry, *Rheol. Acta* **40**, 384-394 (2001).

44. Schwetz, M., Münstedt, H., Heindl, M., Merten, A., Investigations on the Temperature Dependence of the Die Entrance Flow of Various Long-Chain Branched Polyethylenes Using Laser-Doppler Velocimetry, *J. Rheol.* **46**, 797-815 (2002).

45. Hertel, D., Valette, R., Münstedt, H., Three-Dimensional Entrance Flow of a Low-Density Polyethylene (LDPE) and a Linear Low-Density Polyethylene (LLDPE) into a Slit Die, *J. Non-Newtonian Fluid Mech.* **153**, 82-94 (2008).

46. Boukellal, G., Hertel, D., Valette, R., Münstedt, H., Agassant, J.-F., Investigation of LDPE Converging Flows Using Fieldwise Measurements Techniques, *Symposium MS11: Processing of Polymers, Int. J. Mater. Form.* **1**, 687-690 (2008).

47. Musil, J., Zatloukal, M., Gough, T., Martyn, M., Investigation of Vortex Development during Polymer Melt Flows by Flow Birefringence, *AIP Conference Proceedings* **1375**, 14-25 (2011).

48. Zatloukal, M., Chaloupkova, K., Hertel, D., Münstedt, H. Effect of die geometry and extensional rheological properties on vortex development in rectangular dies, Annual Technical Conference - ANTEC, Conference Proceedings, 4, pp. 1938-1942 (2007).

49. Mitsoulis, E., Schwetz, M., Münstedt, H., Entry Flow of LDPE Melts in a Planar Contraction*, J. Non-Newtonian Fluid Mech.* **111**, 41-61 (2003).

50. Martyn, M. T., Spares, R., Coates, P. D., Zatloukal, M., Imaging and Analysis of Wave Type Interfacial Instability in the Coextrusion of Low-Density Polyethylene Melts, *J. Non-Newtonian Fluid Mech.* **156**, 150-164 (2009).

51. Gabriel, C., Kaschta, J., Münstedt, H., Influence of Molecular Structure on Rheological Properties of Polyethylenes I. Creep Recovery Measurements in Shear, *Rheol. Acta* **37**, 7-20 (1998).

52. H. Janeschitz-Kriegel, *Polymer Melt Rheology and Flow Birefringence*, New York: Springer-Verlag, 1983.

53. Fuller, G. G., Optical Rheometry, *Ann. Rev. Fluid Mech*. **22**, 387-417 (1990).

54. G. G. Fuller, *Optical Rheometry of Complex Fluids*, New York: Oxford University Press, 1995.

55. Martyn, M. T., Nakason, C. and Coates, P. D., Stress Measurements for Contraction Flows of Viscoelastic Polymer Melts, *J. Non-Newtonian Fluid Mech.* **91**, 123-142 (2000).

56. Robert, L., Vergnes, B., Demay, Z., Flow Birefringence Study of the Stick-Slip Instability during Extrusion of High-Density Polyethylenes, *J. Non-Newtonian Fluid Mech.* **112**, 27-42 (2003).

57. Den Otter, J. L., Wales, J. L. S., Schijf, J., The velocity Profiles of Molten Polymers during Laminar Flow, *Rheol. Acta* **6**, 205-209 (1967).

58. Clemeur, N., Rutgers, R. P. G., Debbaut, B, Numerical Evaluation of Three Dimensional Effects in Planar Flow Birefringence*, J. Non-Newtonian Fluid Mech.* **123**, 105-120 (2004).

59. White, S. A., Baird, D. G., Numerical Simulation Studies of the Planar Entry Flow of Polymer Melts, *J. Non-Newtonian Fluid Mech.* **30**, 47-71 (1988).

60. Zatloukal, M., Measurements and modeling of temperature-strain rate dependent uniaxial and planar extensional viscosities for branched LDPE polymer melt. *Polymer*, **104**, 258-267 (2016).

Tab. 1: Summary of basic characteristics of used LDPE Lupolen 1840H.

Property	Value	Taken from ref. No.
Density at 25°C (g/cm^3)	0.918	[49]
Melt flow index MFI (g/10min)[a]	1.5	[50]
Weight average molar mass M_w (g/mol)	258000	[49]
Polydispersity index M_w/M_n (-)	16.6	[49]
Melting temperature T_m (°C)	108	[49]
Zero-shear rate viscosity η_0 at 150°C (Pa.s)	54500	[49]
Activation energy E_a (kJ/mol)	58	[49]
Chain branching level CH_3/1000 C (-)	23	[51]
Stress optical coefficient (SOC) at 180°C, x 10^{-9} (m^2/N)	1.34	[50]

[a]ASTM 1238

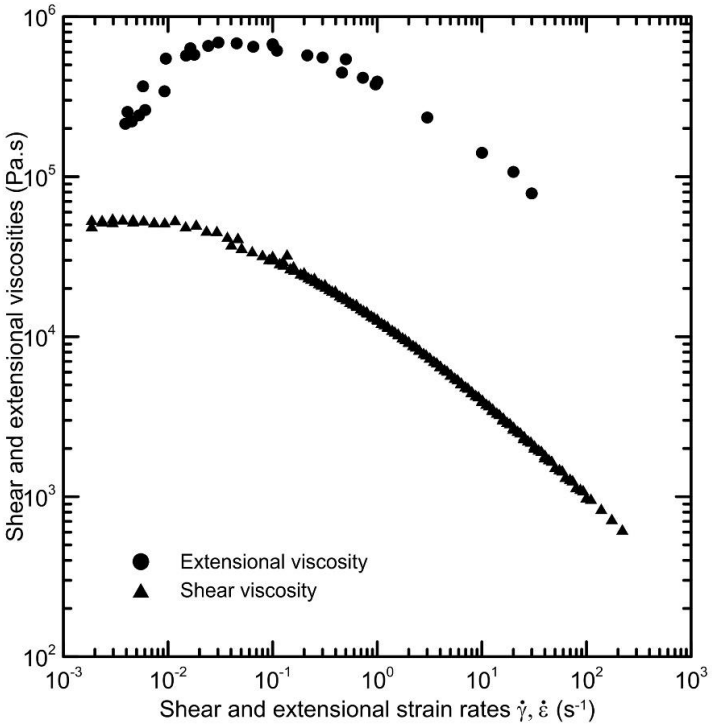

Fig. 1: Shear and uniaxial extensional viscosity data for LDPE Lupolen 1840H at 150°C (data taken from [48]).

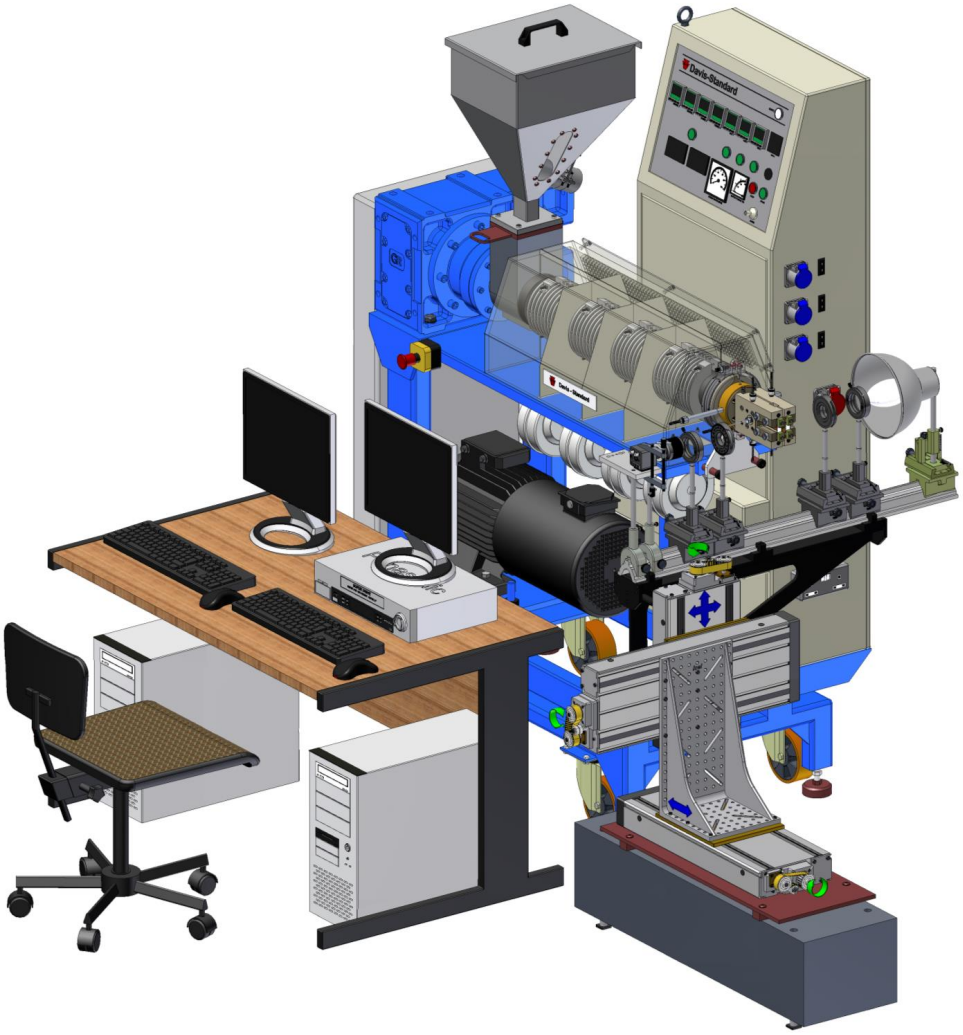

Fig. 2: Overall 3D view of the experimental flow visualization extrusion setup (in scale). More detail information is provided in the Supplementary material.

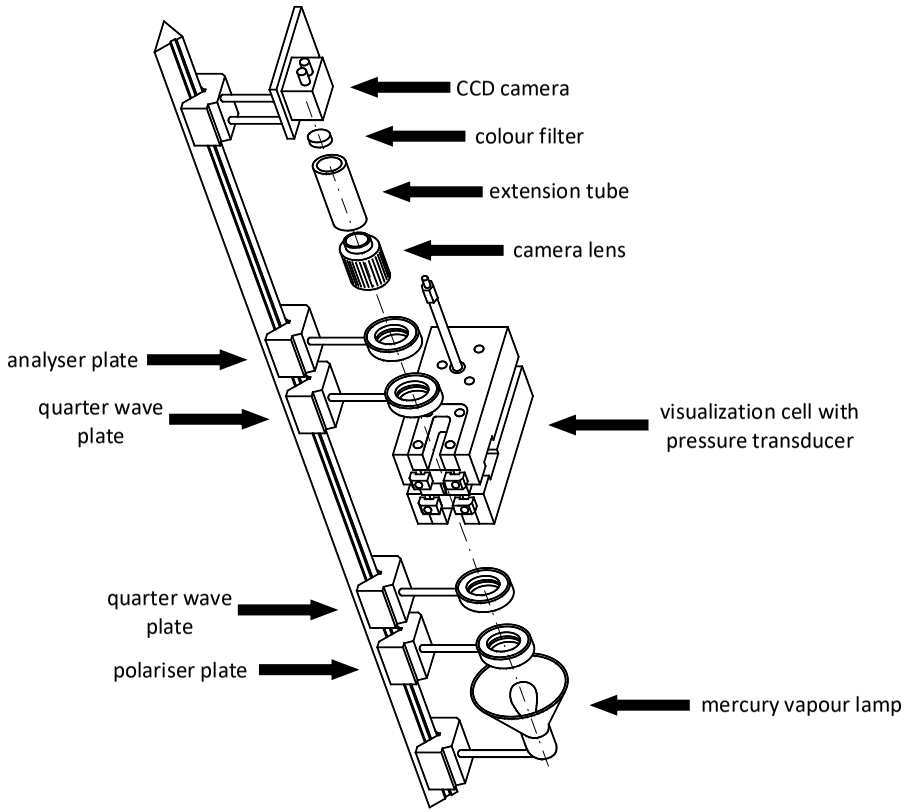

Fig. 3: Schematic view of an optical bench for flow visualization experiments (not in scale).

More detail information is provided in the Supplementary material.

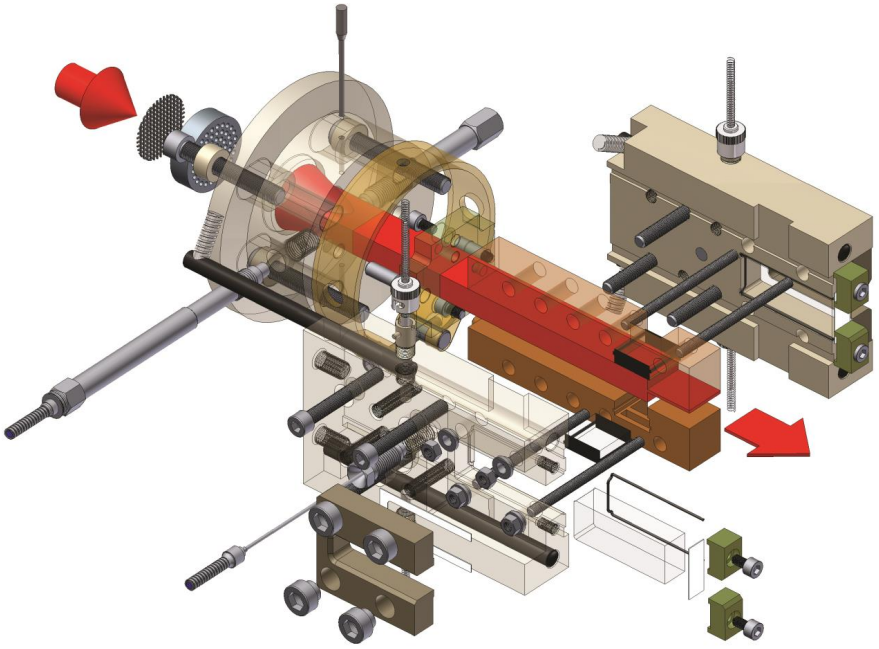

Fig. 4: Partial section view of the used extrusion die (in scale). More detail information is provided in the Supplementary material.

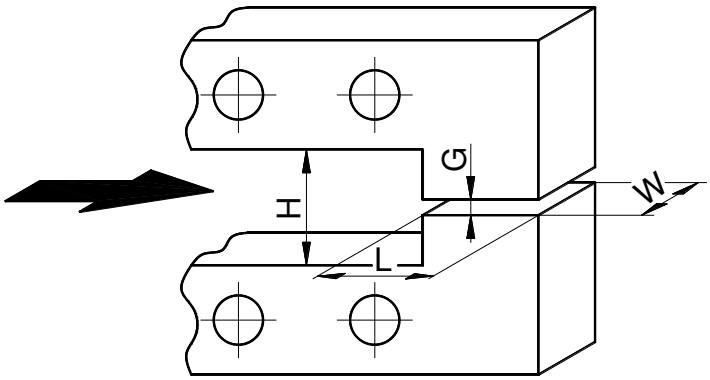

Fig. 5: Schematic view of two inside-die steel inserts determining the flow geometry (not in scale).

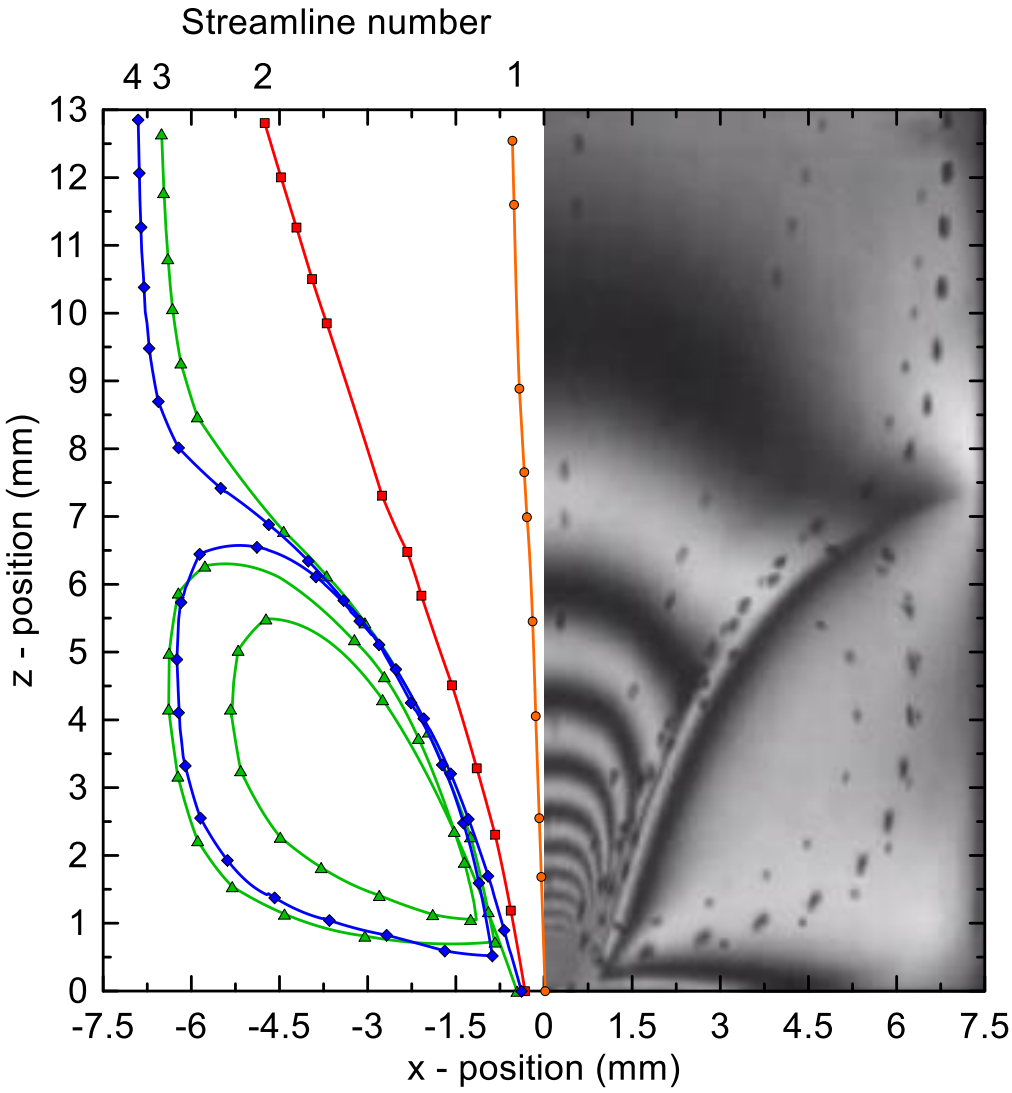

Fig. 6: Particle tracking analysis of 4 different streamlines across the flow geometry for the polymer melt under study at 190°C and the downstream apparent shear rate of 182s^{-1}. Left side – digitized particles positions in Didger^{TM}, right side – stress birefringence field image (multimedia view) with different positions of four tracked particles taken at different durations. The flow direction is from up to bottom.

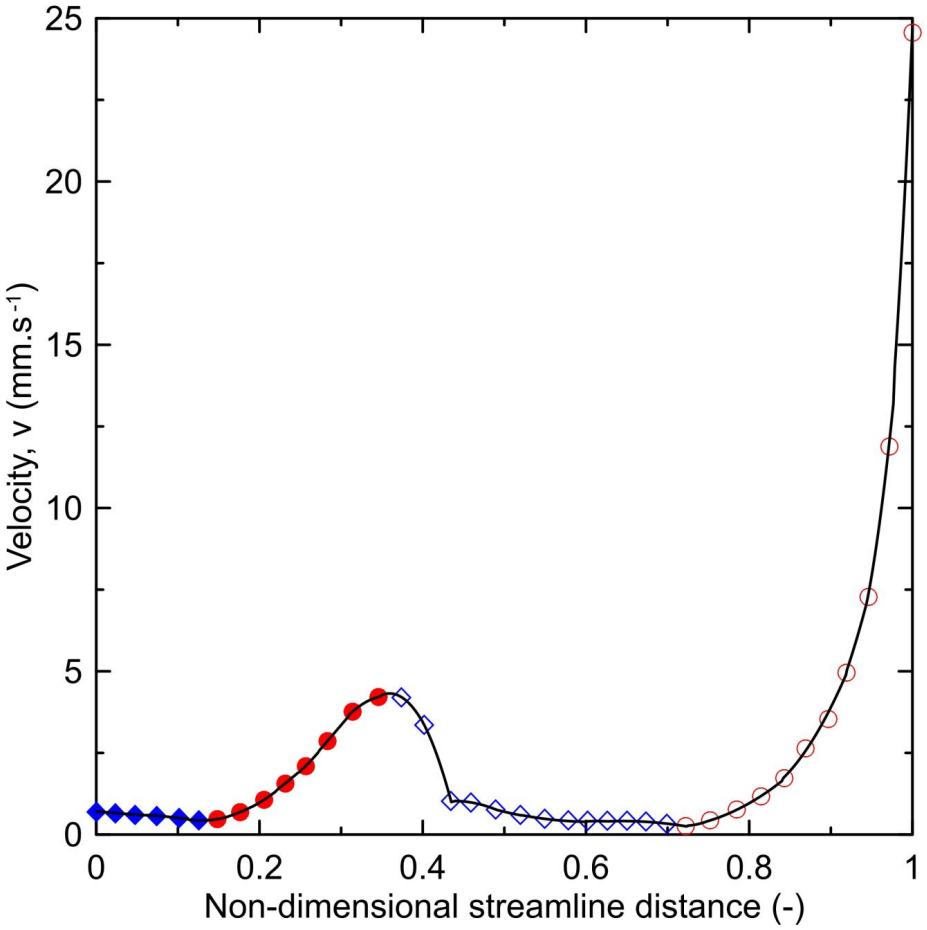

Fig. 7: The velocity along the streamline 4 (see Fig. 6) as a function of the non-dimensional streamline distance. Blue diamonds/red circles represent positions where velocity decreases/increases, respectively. Closed symbols represent positions before particle enters the secondary flow, while open symbols represent particle positions in the secondary flow and after leaving it.

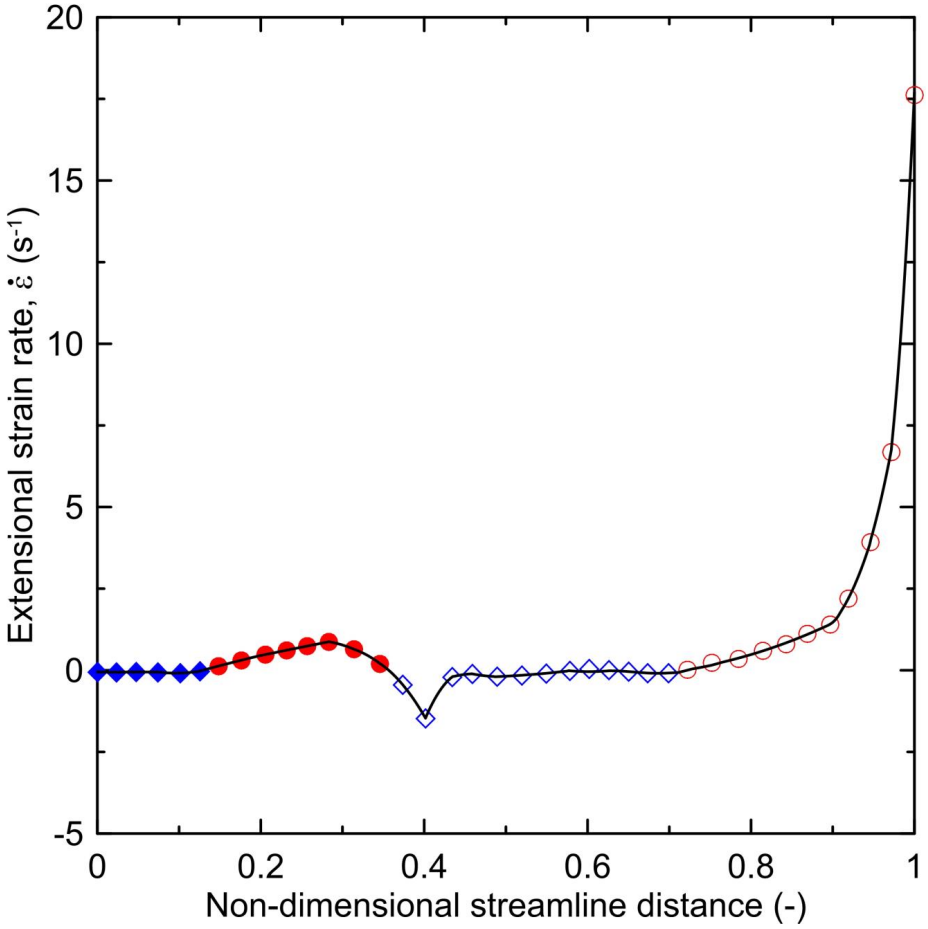

Fig. 8: Extensional strain rate along the streamline 4 (see Fig. 6) as a function of the non-dimensional streamline distance. Blue diamonds/red circles represent positions where the extensional strain rate is negative/positive, respectively. Closed symbols represent positions before particle enters the secondary flow, while open symbols represent particle positions in the secondary flow and after leaving it.

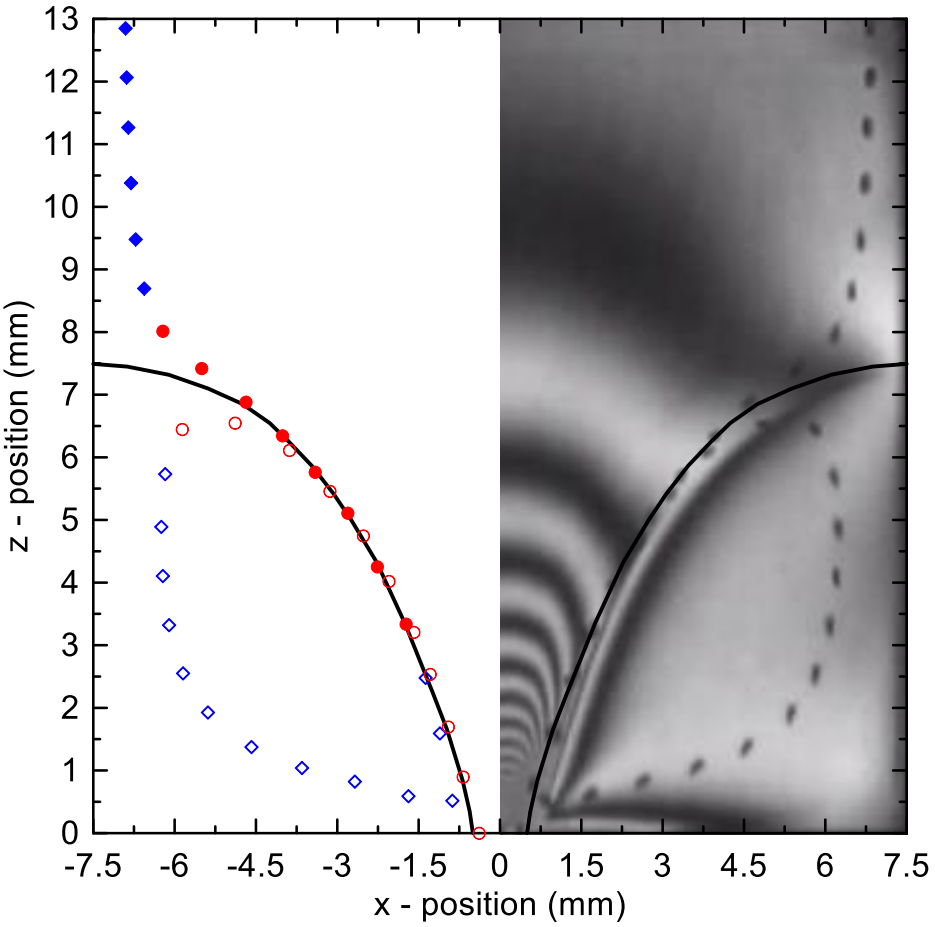

Fig. 9: Particle tracking analysis of streamline 4 (see Fig. 6) for the studied polymer melt at 190°C and the downstream apparent shear rate of 182s^{-1}. Left side – position of digitized particles in Didger^{TM}, right side – image of the stress birefringence field with different positions of the tracked particle taken at different durations. The flow direction is from up to bottom. Blue diamonds/red circles represent positions where the extensional strain rate is negative/positive, respectively. Closed symbols represent positions before particle enters the secondary flow, while open symbols represent particle positions in the secondary flow and after leaving it.

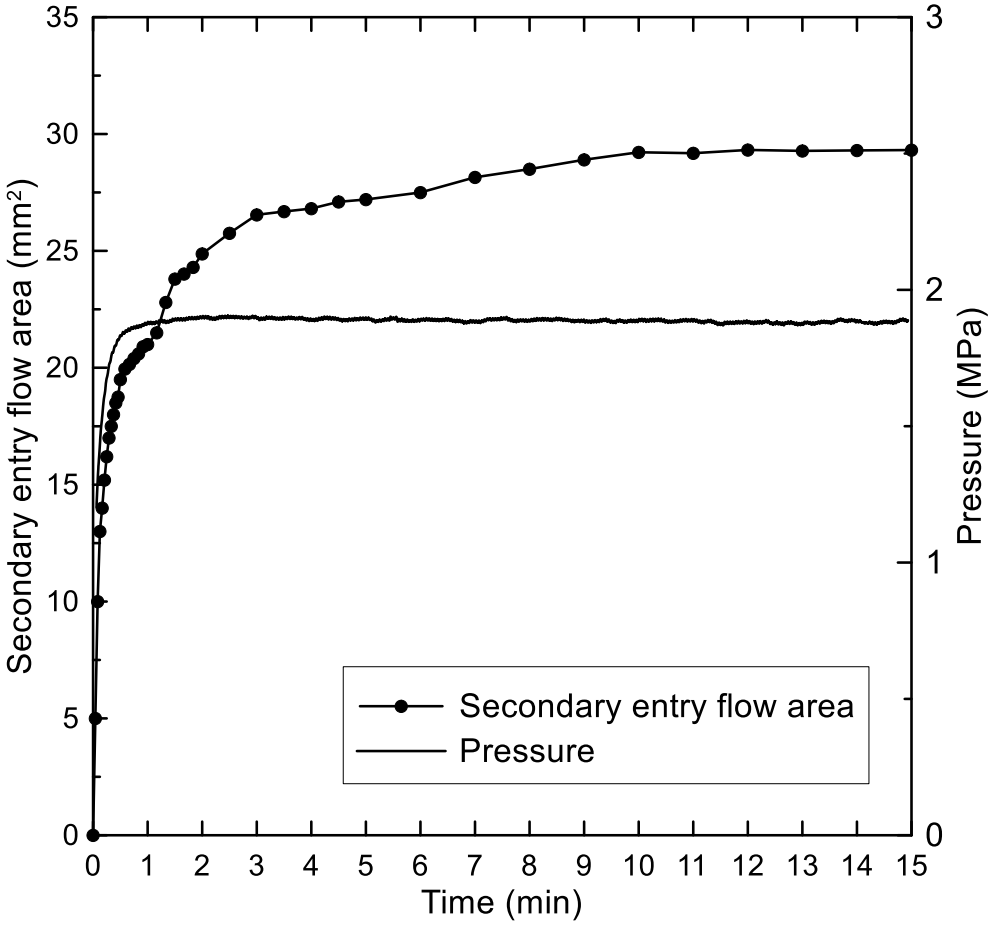

Fig. 10: Time-dependent pressure and secondary entry flow area at minimum ($17s^{-1}$ at 150°C) downstream apparent shear rate collected during FIB video recording.

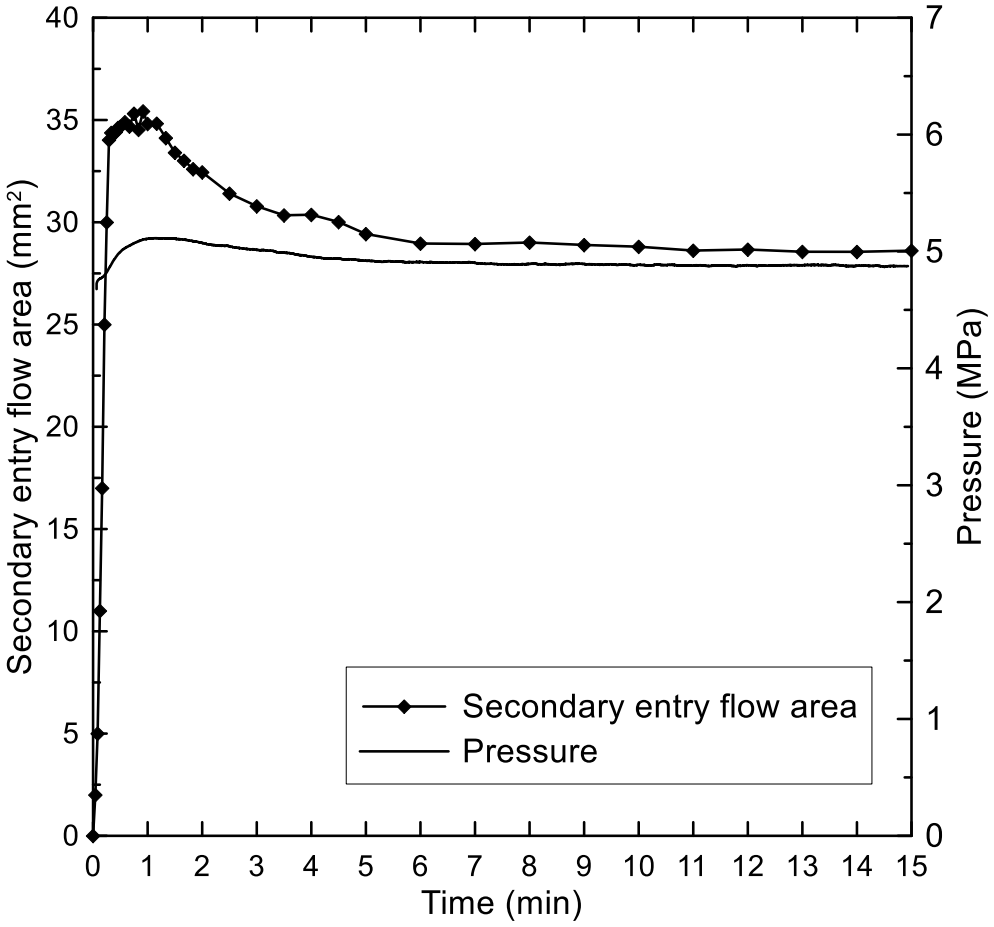

Fig. 11: Time-dependent pressure and secondary entry flow area at maximum ($390s^{-1}$ at 190°C) downstream apparent shear rate collected during FIB video recording.

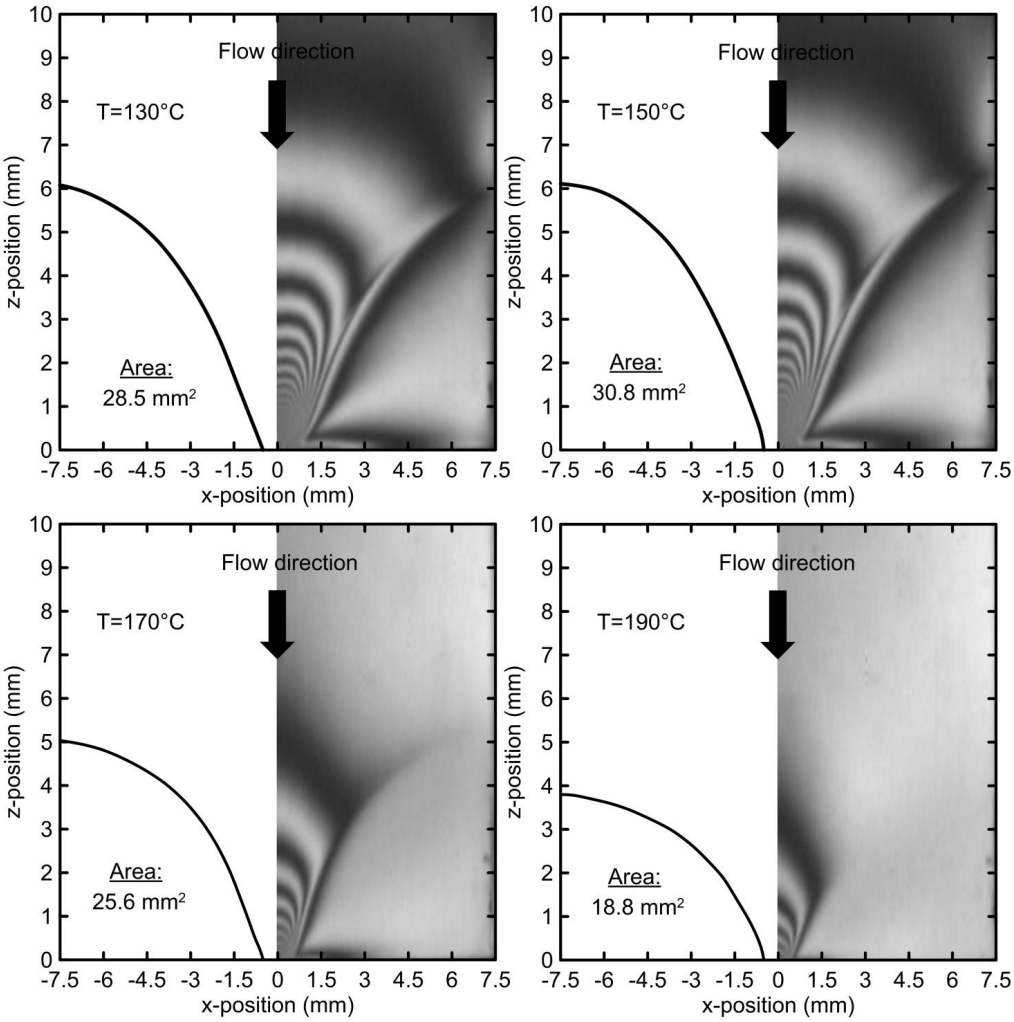

Fig. 12: Visualization of secondary entry flow boundaries at downstream apparent shear rate of $30s^{-1}$ for different processing temperatures (in each graph, the left side represents the secondary entry flow boundary digitized from the stress induced birefringence field, the right side presents the stress induced birefringence field image). Left top: T=130°C (multimedia view); Right top: T=150°C (multimedia view); Left bottom: T=170°C (multimedia view); Right bottom: T=190°C (multimedia view).

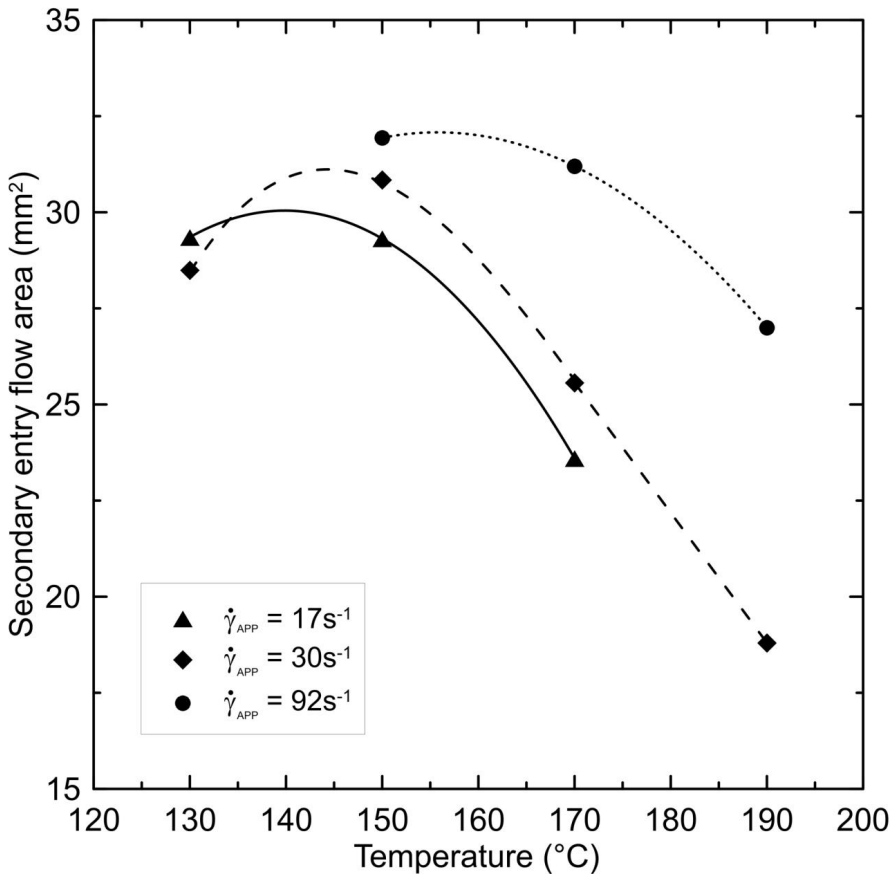

Fig. 13: Secondary entry flow areas as a function of temperature at three different constant downstream apparent shear rates.

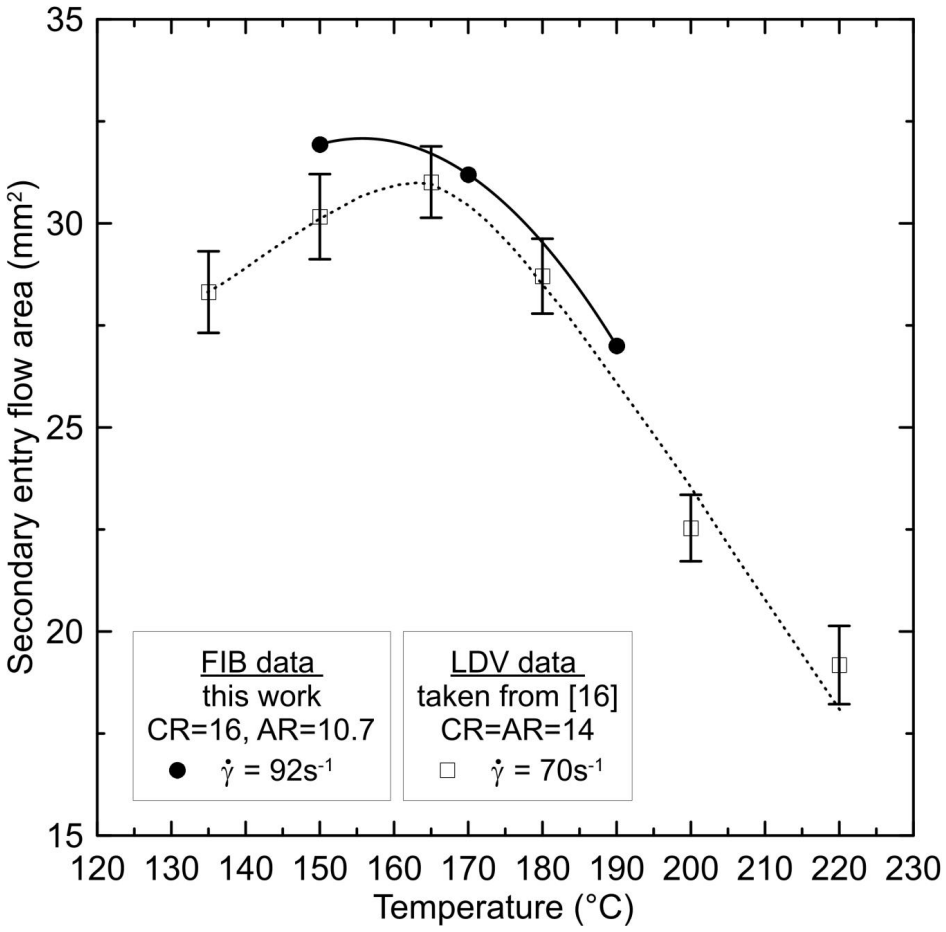

Fig. 14: Comparison of secondary entry flow areas as a function of temperature at similar constant downstream apparent shear rates calculated from stress birefringence fields with open laser-Doppler velocimetry (LDV) data taken from [16].

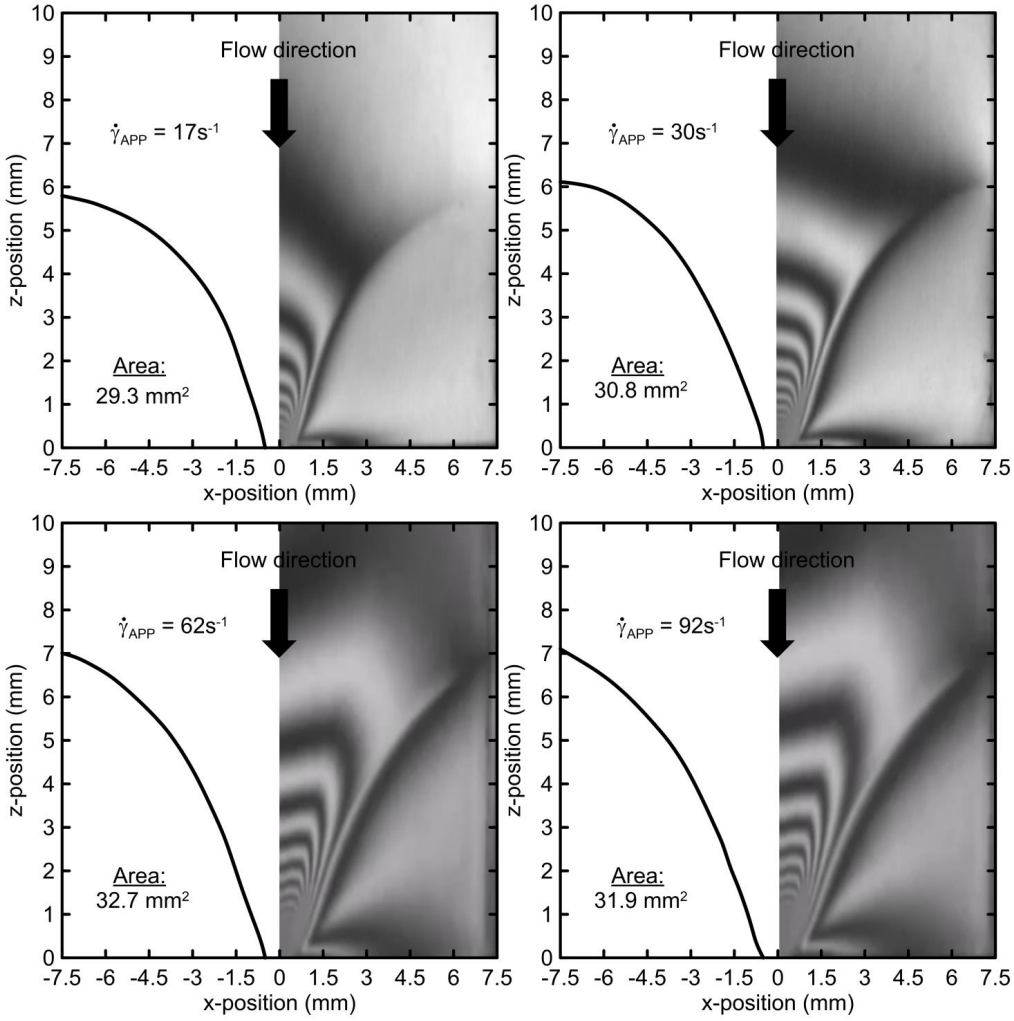

Fig. 15: Visualization of secondary entry flow boundaries at temperature 150°C for different downstream apparent shear rates (in each graph, the left side represents the secondary entry flow boundary digitized from the stress induced birefringence field, the right side represents the stress induced birefringence field image). Left top: $\dot{\gamma}_{app}=17s^{-1}$ (multimedia view); Right top: $\dot{\gamma}_{app}=30s^{-1}$ (multimedia view), Left bottom: $\dot{\gamma}_{app}=62s^{-1}$ (multimedia view), Right bottom: $\dot{\gamma}_{app}=92s^{-1}$ (multimedia view).

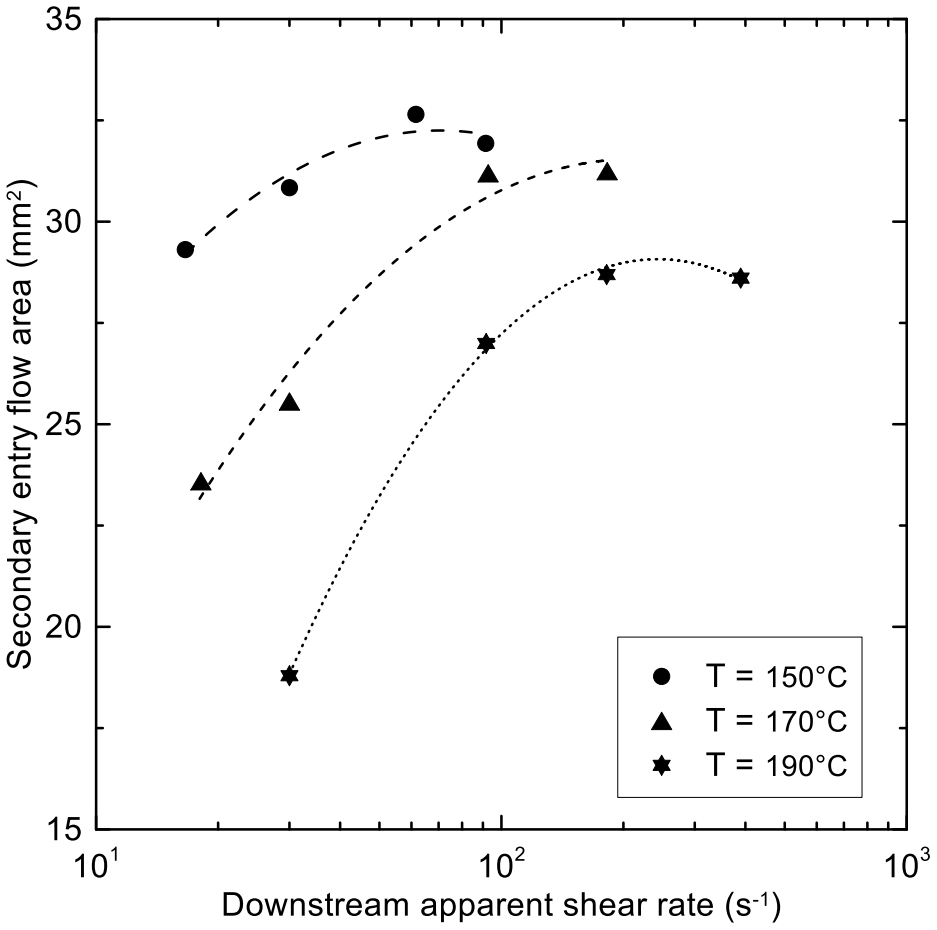

Fig. 16: Secondary entry flow areas as a function of downstream apparent shear rate at three different constant temperatures.

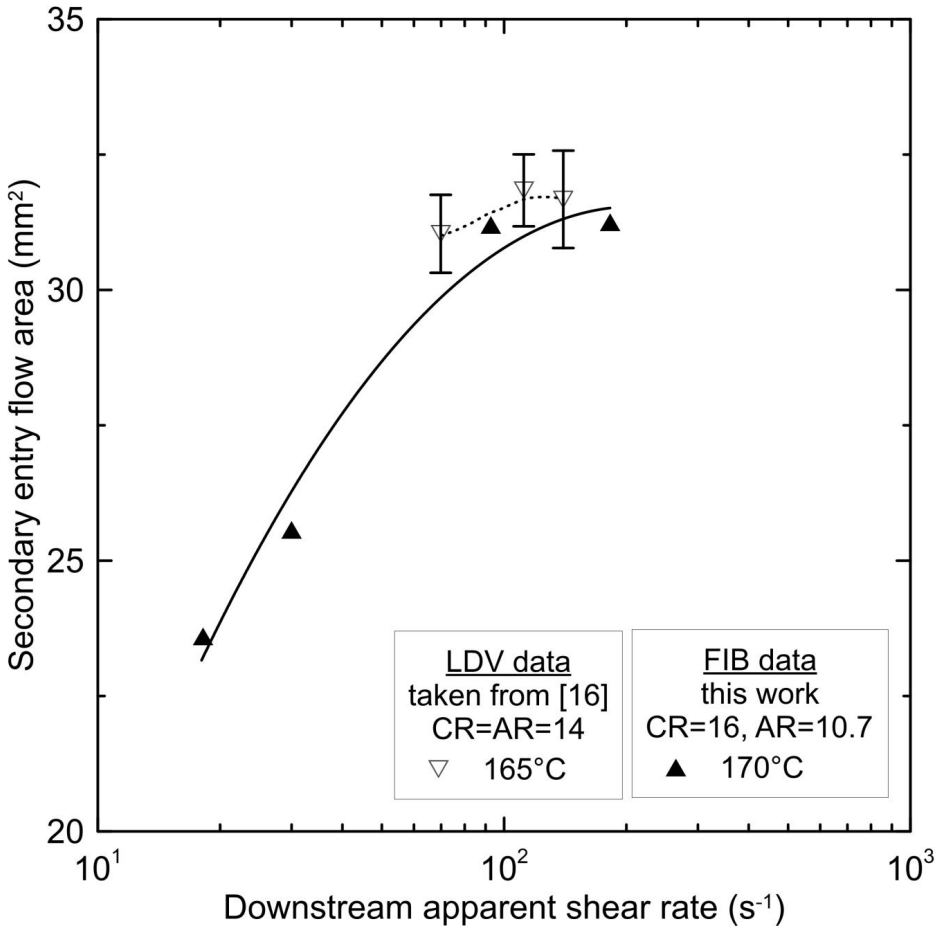

Fig. 17: Comparison of secondary entry flow areas as a function of downstream apparent shear rate at similar constant temperatures calculated from stress birefringence fields with laser-Doppler velocimetry (LDV) data taken from [16].